



<https://doi.org/10.15407/ufm.24.01.005>

M.O. VASYLYEV^{1,*}, B.M. MORDYUK^{1,2,}, and S.M. VOLOSHKO²**

¹ G.V. Kurdyumov Institute for Metal Physics of the N.A.S. of Ukraine,
36 Academician Vernadsky Blvd., UA-03142 Kyiv, Ukraine

² National Technical University of Ukraine
'Igor Sikorsky Kyiv Polytechnic Institute',
37 Peremohy Ave., UA-03056 Kyiv, Ukraine

* vasil@imp.kiev.ua, ** modyuk@imp.kiev.ua

WIRE-FEEDING BASED ADDITIVE MANUFACTURING OF THE Ti-6Al-4V ALLOY. PART I. MICROSTRUCTURE

In recent years, the metal additive manufacturing (AM), also known as 3D printing, is grown massively in the industry. The ability of AM to build parts directly from the digital representation makes it an excellent alternative compared to traditional manufacturing technologies, such as milling, welding, casting, rolling, stamping, forging and turning for rapidly making highly customized parts. Currently, a number of the different powder- and wire-based AM technologies are developed for 3D printing of metals. A number of potential benefits of AM are noted, including the allowance of design freedom, complex parts' production, the material waste and part weight reductions, material use minimization; it also saves the time and money of the production cycle times. Due to the feasibility of the economically producing large-scale metal components with relatively high deposition rate, low machinery cost, high material efficiency, and shortened lead time as compared to the powder-based AM, the wire-based AM significantly attracted in the industry and academia due to its ability to produce the large components of the medium geometric complexity. During this AM process, the wire is fed by the controlled rate into the melt pool produced by the electric arc, laser or electron beam as the heat source. In the past few decades, the basic research and development efforts are devoted to the wire-based 3D printing parts made of Ti-6Al-4V alloy, which has been widely investigated and used in different fields such as aerospace, automotive, energy, marine industries and in addition to the prosthetics and the orthopaedic

Citation: M.O. Vasylyev, B.M. Mordyuk, and S.M. Voloshko, Wire-Feeding Based Additive Manufacturing of the Ti-6Al-4V Alloy. Part I. Microstructure, *Progress in Physics of Metals*, **24**, No. 1: 5-37 (2023)

© Publisher PH "Akadempriodyka" of the NAS of Ukraine, 2023. This is an open access article under the CC BY-ND license (<https://creativecommons.org/licenses/by-nd/4.0/>)

implants. Numerous studies in recent years on the influence of the 3D printing parameters have shown significant difference in the mechanism and kinetics of the microstructure formation in the Ti–6Al–4V alloy samples compared to traditional technologies. It is well investigated that the mechanical properties of such alloy are dependent on the solidification macro- and microstructure, which is controlled by the thermal conditions during 3D printing. In the present review, the main microstructural characteristics, which determine the mechanical properties of the two-phase Ti–6Al–4V alloy, are analysed for the samples obtained by wire-feed 3D printing with various sources used for the wire melting, namely, the electric arc, the laser, and the electron beam. At first, the review introduces the links between the process parameters, resultant microstructures, especially, the morphology, the size and the quantitative ratio of the α and β grains in the as-printed Ti–6Al–4V alloy samples. However, the metallic products manufactured by a vast majority of the AM processes need to be post-processed by heat treatment and/or hot isostatic pressing, which are also discussed in this review.

Keywords: additive manufacturing, 3D printing, Ti–6Al–4V alloy, microstructure, electric arc, laser, electron beam, crystallization, heat treatment, mechanical properties, industry.

1. Introduction

Additive manufacturing (AM), also known as 3D printing, is a fabrication technology where the three-dimensional solid object (parts, details) is built in an incremental layer-by-layer, point-by-point or line-by-line manner without deformation or material removal using the Computer-Aided Design (CAD) software. After the 3D printing, the certain solid object can consist of several thousand layers with a thickness of 20–200 μm [1–3]. AM has several capabilities such as creating the shape complexity, hierarchical complexity, material complexity, and functional complexity.

The first step to the commercialization of AM is related to the patent by Chuck Hull, who founded the company in 1984 [4]. Nowadays, AM is accepted as the novel candidate for the fabrication of the different material 3D products, and it is at the forefront of the new industrial revolution and receiving increasing attention around the world. Significant advancements of AM are the wide range of materials able to be utilized including ceramics, chemicals, composites, concrete, food-stuffs, metallic materials (including Al alloys, Co–Cr alloys, Cu, Au, Fe-alloys (including stainless steels), Mg, Ni and Ti-based alloys), paper, plastics, sandstone, silicones, wax and wood [5–9].

One of the most important modern directions of AM is metal 3D printing. AM of metal products is especially important because metals and alloys are still the main industrial construction materials. AM is very competitive compared to conventional manufacturing techniques such as milling, welding, casting, forming, forging, and turning owing

to the capability of the metal 3D printing to fabricate the three-dimensional metal complex geometries parts, with significant time, cost and waste material reduction. Metal 3D printing technology has been around since the 1980s. The first fully dense metal 3D printed parts came about when in 1990–2004 the GmbH Electro Optical Systems (EOS) suggested the highly productive direct metal laser sintering (DMLS) systems using metal 3D printing. At present, a growing number of metals and metal alloys are used for industrial-grade 3D printing. Due to rapid technological advancement, metal 3D printing has grown massively in recent years. Using the metal 3D printing method for many applications allows companies in the aerospace, automotive, defence, and medical industries to produce parts with complex geometries unachievable using traditional manufacturing methods such as casting, fabrication, machining, rolling, stamping, *etc.*

Currently, a number of the different AM technologies for metals 3D printing have been developed. They differ in consumable materials, such as powder, wire, or powder-binder mixture; the source of heating of the consumable materials, such as laser, electron beam, plasma, electric arc; a method of the layer forming – selective melting (sintering) of the prepared powder bed, direct deposition of the powder or wire on the previous layer. However, most of AM-produced metals need to be subjected to post-processing treatment, such as heat treatment and hot isostatic pressing or peening, to improve their mechanical properties (yield, tensile strength, and fatigue life).

The following most important AMs can be distinguished for metal 3D printing, namely selective laser sintering (SLS), selective laser melting (SLM), and electron beam melting (EBM). When choosing one or another AM method, it is necessary to take into account that there is a trade-off between the limiting part size, deposition rate, and layer height resolution. For example, to produce economically large airframe parts, high deposition rates of kilograms per hour and building envelopes of several meters are required. In this case, the wire-fed AM method with higher power heat sources is most suitable for such applications. Currently, a low-cost wire-based AM process that exploits standard welding technology has become of interest to the industry. In particular, this technique has been presented to the aerospace manufacturing industry as a unique low-cost solution for manufacturing large thin-walled structures by significantly reducing both product development time and ‘buy-to-fly’ ratios [10–14].

Excellent strength-to-weight ratio, superior biocompatibility, low elastic modulus, and exceptional corrosion resistance of the α - β titanium alloy (Ti-6Al-4V) are well known. They are determinative factors facilitating a wide use of Ti-6Al-4V alloy in load-bearing applications in aeronautics, such as gas turbines, jet engines, and other components

in the aerospace industry, automobile, biomedical, energy and chemical industries. Additionally, Ti-6Al-4V alloy is critically sought after in naval aviation applications, where the combination of the high corrosion properties along with superior specific strength is extremely demanded. However, traditional machining is very prolonged and very costly. Recent studies and practical results have shown that modern AM is able to eliminate these difficulties. Therefore, innovative manufacturing now routes are required.

It is well known that the optimal strength and ductility of the Ti-6Al-4V alloy products can be achieved by appropriate thermal or thermo-mechanical treatment, which determines the morphology of the main structural components of the alloy, namely, α and β phases. For traditional technologies, these processes have been thoroughly studied. Numerous studies of recent years on the influence of the methods and parameters 3D printing have shown the significant difference in the mechanism and kinetics of the microstructure formation in the Ti-6Al-4V alloy compared to traditional technologies. The present review analyses the works dedicated to different options of the wire-feed AM of the titanium alloy Ti-6Al-4V.

Below, there are the main results of the most systematic structural studies of the samples of Ti-6Al-4V alloy obtained by wire-feed AM with various sources of the wire melting, namely, arc, laser, and electron beam.

2. Wire + Arc Additive Manufacturing

Currently, wire + arc additive manufacturing (WAAM) is the most effective alternative to traditional subtractive manufacturing for fabricating parts made of aerospace alloys. This method of AM is the subject of the largest number of research papers related to 3D printing of the Ti-6Al-4V alloy. WAAM is one type of metallic AM, which combines the arc-welding torch as the heat source and metallic wires as feeding materials. The initial WAAM idea can be dated back to 1926 when Baker [15] proposed to use simple arc welding to deposit metal ornaments. After around one century of development, WAAM becomes mature and indispensable. With the assistance of automation and digitization techniques, it has been employed in various industrial fields [16–19].

WAAM is amongst the most affordable AM because it is based on inexpensive Gas Tungsten Arc Welding (GTAW) technology [20]. It is important to note that GTAW also referred to as tungsten inert gas (TIG), is one of the most common welding methods used for titanium and its alloys. GTAW is based on the joining of two materials, which are heated, with the electric arc established between the W non-consumable electrode and the parts to be welded. The WAAM technology utilizes the

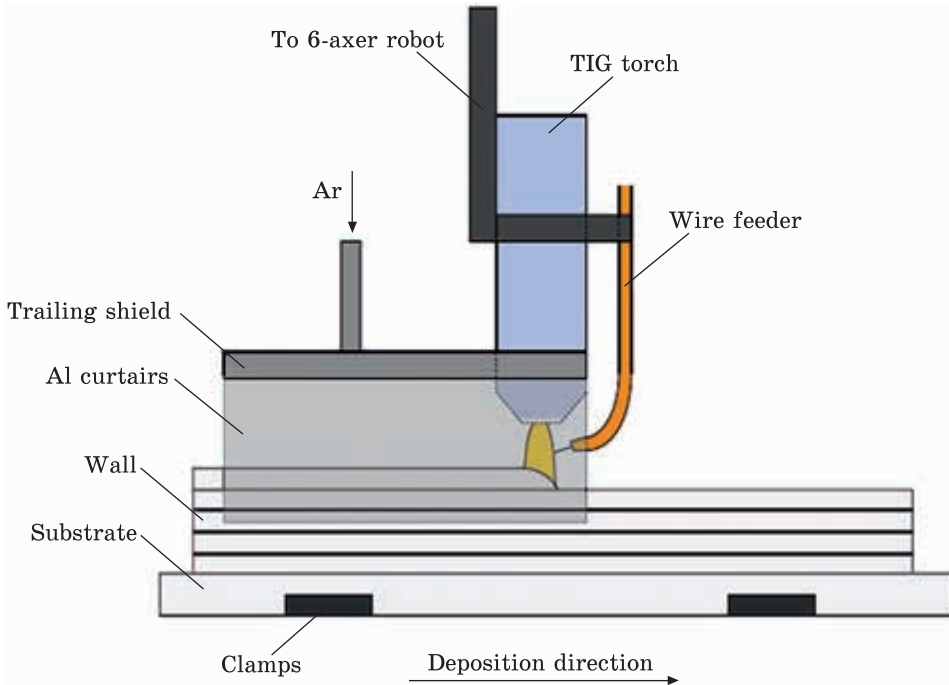


Fig. 1. Schematic of the WAAM setup [13]

electric arc as a heat source and wire for its feedstock. The electric arc is formed in the Ar medium when the W electrode and the wire part are brought close to each other. Thus, this AM combines the arc-welding torch and the external wire-feeding unit with 6 axes robot-linked to the 2-axis table (Fig. 1) [13, 21–23]. Due to the highly complex nature of WAAM, many different aspects of the process need to be studied to get the desired microstructure and mechanical properties, and the high efficiency of the final large-scale products. Particularly, the following WAAM process parameters are important: a pulsed direct current, pulse frequency, pulse duration, arc voltage, travel speed, scanning speed, a flow rate of argon in W torch, a flow rate of Ar in the trailing shield, W electrode diameter, wire diameter, wire feed speed, the distance between the electrode and workpiece, angle between the electrode and the filler wire, dwell time between layers, deposited layer height, number of the deposited layers, trailing shield gas flow rate.

Below are the main results of the macro- and microstructure study of the Ti-6Al-4V alloy samples after 3D printing by WAAM.

It was studied that the macro- and microstructure of the Ti-6Al-4V alloy samples as printed by WAAM is very different from that of the conventional casting or forging alloys. The main reason for this effect is the rapid heating and solidification of the printed layers and the sub-

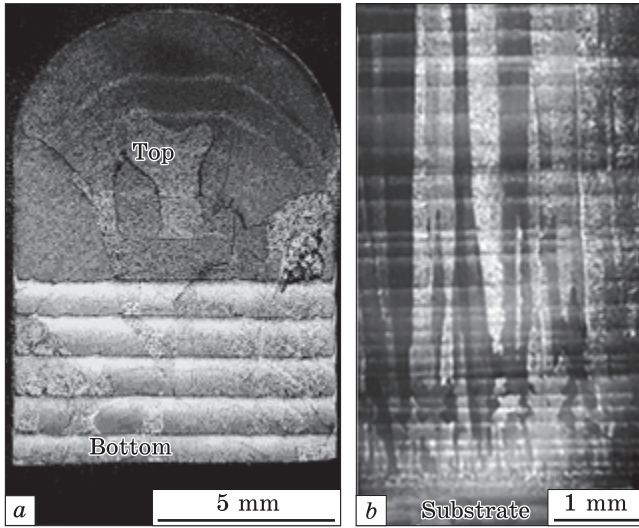


Fig. 2. The typical macrostructure in the etched cross sections of the Ti-6Al-4V alloy samples as-printed by WAAM reported in [26] (a) and [29] (b)

sequent repeated thermal cycling that occur as the consequence of the layer-by-layer 3D build process [24, 25].

Figure 2 shows the typical macrostructure in the etched cross-sections of the Ti-6Al-4V alloy sample as printed by WAAM [26, 29]. One can see in the cross section two differently appearing regions: the bottom region, which is characterized by bands parallel to the base plate, and the top region, where these parallel bands are absent. It is obvious that the parallel bands are not directly related to the deposition layers, since they do not coincide with them. For example, Table 1 shows the geometric dimensions of the regions depending on the 3D printing parameters [18]. The height of these top regions is not very sensitive to the height of the whole component.

Many studies have found that the macrostructure of the WAAM Ti-6Al-4V is characterized by the epitaxial growth of the striking coarse elongated columnar prior-β grains that developed during solidification and grew from the substrate across the deposited layers [28, 29]. They extended to the top of the sample and had an average grain width

Table 1. The deposition parameters and the resulting geometry [27]

Deposition parameters			Geometry		
Current, A	Wire feed speed, m/min	Travel speed, m/min	Height, mm	Band width, mm	Height of top region, mm
150	2.1	0.30	120	8.8	8.8
183	2.2	0.25	70	9.5	8.7
163	1.8	0.30	70	8.8	8.2
165	1.4	0.25	70	9.5	8.8

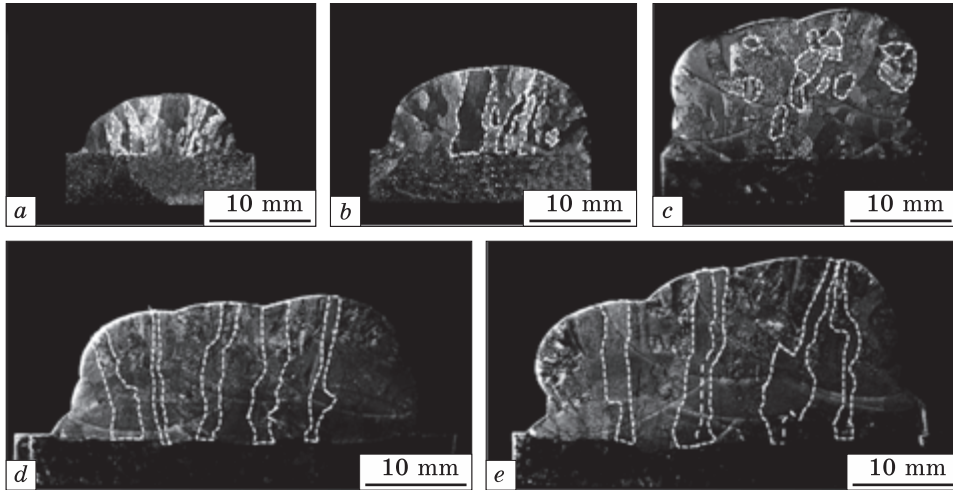


Fig. 3. Macroscopic grain morphology of the blocks manufactured at the wire feed speed (WFS) of (a) 100 cm/min; (b) 200 cm/min; (c) 300 cm/min; (d) 400 cm/min and (e) 500 cm/min [30]

of 1 to 2 mm. Furthermore, the preferred growth direction of the prior β columnar grains was almost perpendicular to the substrate. The colour variation in the columnar grains is caused by their different crystallographic orientations. As shown in Fig. 2, once established, the columnar prior- β grains thus continue to grow across each deposited layer from the substrate to throughout the whole sample to form one grain. Generally, the growth of such grains depends on thermal gradient G (K/m) and grain growth rate R (cm/s). The G and R in WAAM almost keep constant because it is the single-pass and multi-layer reversed deposition process.

The morphology of the columnar prior- β grains significantly depends on WAAM parameters. One of the most important of these parameters is wire feed speed (WFS). As an example, Fig. 3 shows the optical microscopy of the specimens' grain morphology manufactured at different WFS. One can see that with the increase of WFS, the width and height of the printed block increases accordingly [21]. It can be seen clearly that the outline of each deposited bead, indicating the molten pool (WMP) size, tends to increase. The width of WMP, total width and total height of the deposition, layer thickness, and grain width are measured as shown in Table 2. The WMP width of the molten pool can be obtained under each wire feed speed WFS condition [21].

Generally, the microstructure of the printed Ti-6Al-4V alloy samples is dependent on the peak temperature, time at the temperature, and the cooling rate during the multiple thermal cycles experienced by each layer of the deposited material. In particular, the meta-stable micro-

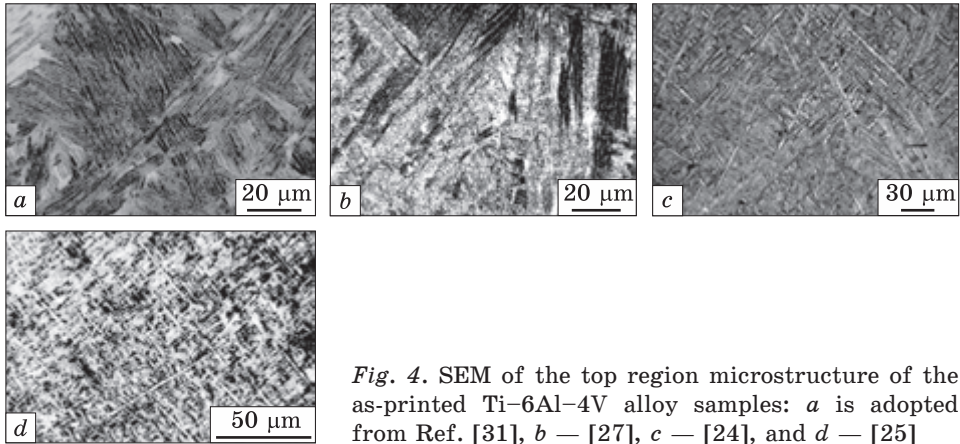


Fig. 4. SEM of the top region microstructure of the as-printed Ti-6Al-4V alloy samples: *a* is adopted from Ref. [31], *b* – [27], *c* – [24], and *d* – [25]

structures of the printed product by WAAM also depend on its complex thermal history during the fabrication process, which involves repeated heating and cooling. The more detailed studies of anisotropic microstructures performed in the recent years are presented below.

As was noted above, the top and bottom regions of the as-printed samples have different macromorphologies. For all components, the microstructure in both regions mainly consists of the Widmanstätten morphology. These are the α -phase lamellae in the β -phase matrix, exhibiting either the basket weave or the colony structure, which are different in the size in both regions.

Generally, the un-banded region at the top of the printed sample consists of the so-called Widmanstätten structure with the needle-like α -phase lamellae in the β -phase matrix exhibiting the basket-weave structure and some α lamellae (Fig. 4) [24, 25, 27, 31]. The as-printed microstructure inside the prior- β grains is characterized mainly by continuous prior- β grain boundary α -phase (α_{GB}), Widmanstätten grain boundary α -phase (α_{WGB}), and the intragranular basket-weave α -phase. The α_{GB} and α lathes have the average widths of 0.69 and 0.95 μm , respectively.

Table 2. Macroscopic parameters at different WFS [30]

WFS, cm/min	WMP, mm	Total width, mm	Total height, mm	Layer thickness, mm	Average grain width, mm
100	7	14.5	5.7	1.9	0.72
200	10	19.0	8.1	2.7	0.92
300	14	23.1	12.3	4.1	0.98
400	19	32.8	13.5	4.5	1.05
500	22	35.2	16.5	5.5	1.23

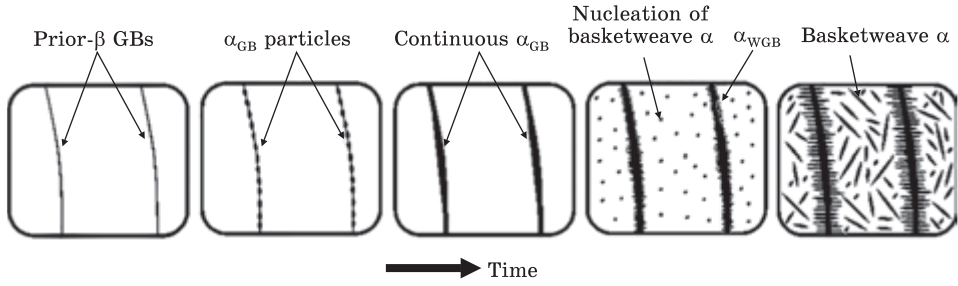


Fig. 5. Schematic illustration of nucleation and growth of α_{GB} , α_{WGB} , and basket weave α during WAAW [31]

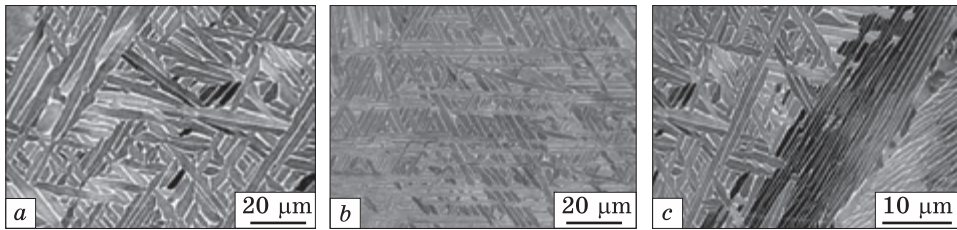


Fig. 6. SEM images of the bottom region: *a* — [35], *b* — [27], *c* — [35]

Besides, under fast cooling of the single-pass deposition, the high-temperature phase β can be transformed to the α -phase of different morphology and brittleness including martensite α' , martensite α'' , acicular α , needle-like secondary α , grain boundary α , and fine basketweave structure (Widmanstätten α) [32]. When the $\beta \rightarrow \alpha + \beta$ transformation takes place, α phase is preferential homogeneously formed from prior- β grain boundaries because of the relatively lower activation $\beta \rightarrow \alpha + \beta$ energy needed for the α phase nucleation at the prior- β grain boundaries [33]. Many α_{GB} particles can easily grow to connect to become continuous [34]. Then, the lamellar α colonies grow into the prior- β grains starting from the α_{WGB} nucleates. Also, the large cooling rate from the β -phase field to the ' $\alpha + \beta$ '-phase field is the consequence of the high undercooling and large nucleated driving force within the prior- β grains and a large amount of the intragranular α nuclei are formed simultaneously, and these α nuclei grow to become intragranular basketweave α . Due to the competition of the growth processes, the growth of α_{WGB} was blocked by the intragranular basketweave α -phase. Figure 5 schematically shows the microstructure evolution during WAAM [31].

Figures 6 shows the several examples of the typical coarse basketweave Widmanstätten microstructures with α phase lamellae most frequently observed in the bottom region of WAAM-produced material [27, 35]. The main differences between the bottom and top areas are the following: the bottom area contains alternating bands perpendicular to the

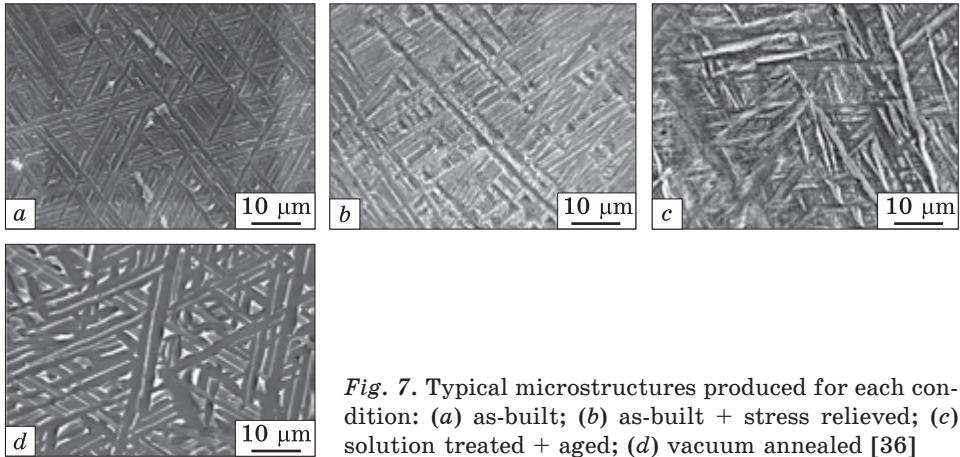


Fig. 7. Typical microstructures produced for each condition: (a) as-built; (b) as-built + stress relieved; (c) solution treated + aged; (d) vacuum annealed [36]

build direction, while such bands are conversely absent in the top region that contains much finer lamellae and needle-like precipitates than those in the bottom one. The reason for these differences in microstructure relates to the rapid heating–cooling cycles during printing every new layer in the WAAM process.

It is well established that the complex thermal cycles experienced by the deposited metal always cause the printed component to have the non-uniform distribution of the microstructure, mechanical properties, and large residual stress. To reduce the anisotropy of the microstructure, the cracking initiation probability, mechanical properties, and residual stresses of the WAAM-printed objects, they should be post-processed. At present, the focus is on two types of such processing, namely, post-heat treatment (PHT) and the post-hot isostatic pressing (PHIP). Many researchers have shown that post-build processes are effective in improving the microstructure and ductility at the expense of some strength of the Ti–6Al–4V samples produced by WAAM. This is very important in light of the coarser microstructure produced by this AM. This part of the present review aims to compare the microstructures and mechanical properties of the Ti–6Al–4V samples printed produced by WAAM that are subjected to different post-printing treatments.

One of the heat treatments used for the printed samples of Ti–6Al–4V alloy that contained coarse prior- β grains often exceeding several millimetres in size is solution treatment and ageing (STA) [36]. This treatment involves the solution treating to develop the larger β -phase fraction followed by quenching and subsequent ageing to decompose the unstable β and stimulate the higher strength. In work [36], the post-heat treatment was selected as the final condition to evaluate the microstructure and the mechanical properties of the Ti–6Al–4V alloy samples

produced by WAAM. All of the analysed heat-treated conditions are shown in Table 3.

It was concluded that PHT did not change the morphology or size of the prior- β grains, but there was a significant change in the size of the α -grain structure (Fig. 7). After all used PHT, the microstructure is predominately Widmanstätten/acicular- α . However, the thickness of the α -laths (and β -regions) varies significantly. On the other hand, the solution heat treatment leads to the higher fraction of β -phase, which is then quenched to either save the supersaturated β -phase or transform to the α' martensite. At subsequent ageing, these metastable phases decompose to form fine acicular α . The different thermal processes were found to influence directly the mechanical properties through a Hall-Petch relationship with the α -grain size.

The study [32] focuses on the influence of PHT on the microstructure, mechanical properties, and residual stress of the Ti-6Al-4V samples produced by WAAM. Table 4 shows the phase compositions and appropriate mechanical properties of 3D-printed material after different heat-treatments. As seen, most WAAM-fabricated samples exhibit a lower strength and higher elongation in the vertical (build) direction than those in the deposition direction. The reduced ductility is observed to be associated with the presence of more brittle phases as Widmanstätten α' or acicular α . As noted in the work [23], the large columnar β -phase promotes good ductility but reduced strength. A multi-stage PHT yields a good combination of the strength and ductility of the printed samples (Table 4). Generally, the single-stage PHT improves the ductility, enhances strength, eliminates the brittle phase, and refine the grain (e.g., the columnar prior β -phase).

In addition to post-heat treatment, other post-treatment techniques, like hot isostatic pressing (HIP), the manufacturing process, which utilizes elevated temperature and isostatic gas pressure, can be used to enhance the performance of 3D printed titanium alloy products. For the first time, was by manufacturers around the world successfully used the HIP process in powder metallurgy. Recently, HIP started to be used in various AM methods to homogenize the microstructure, eliminate the

Table 3. Summary of the different PHT conditions investigated [36]

Condition	Details
As-printed	Residual stresses are maintained
As-printed + stress relief	Stress relieved at 753 K for 2 h
Vacuum annealing	1200 K for 2 h dwell with 5 K/min heating and cooling rate
Solution treatment + age	Solution treated at 1240 K for 1 h, water quenched then aged at 868 K for 2 h and air cooled

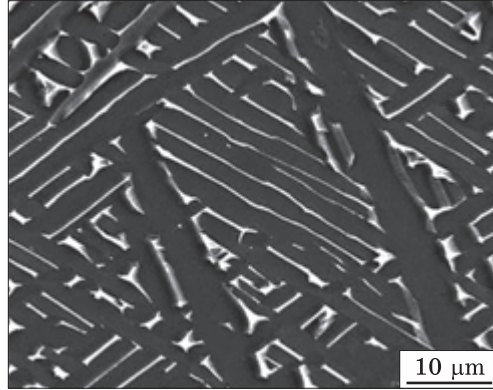
microspores and remove defects, such as nitrides, oxides, and carbides, and substantially increase the density, ductility, fatigue resistance and fatigue toughness of the 3D printed parts owing to the combination of the plastic deformation, creep, and diffusion bonding [32, 36–41]. Thus, HIP improves the 3D materials' mechanical properties and potentially workability, particularly, for aerospace applications and medical implants.

Table 4. Microstructure and mechanical properties of Ti–6Al–4V alloy samples printed by WAAM [32]

State	Microstructure	YS, MPa	UTS, MPa	El, %
AS-printed	Widmanstätten α + banded coarsened lamella α	803	918	14.8
	Prior β grains + fine Widmanstätten α	710	820	7.18
	Prior β + continuous grain boundary α + Widmanstätten grain boundary α + intragranular basket weave α	746	847	12.2
AN (600 °C/4h/AC)	Prior β + continuous grain boundary α + Widmanstätten grain boundary α + intragranular basket weave α	772	854	11.8
AN (850 °C/2h/AC)	Prior β + continuous grain boundary α + Widmanstätten grain boundary α + intragranular basket weave α + secondary α	734	846	13.6
HT (930 °C/1h/AC + 550 °C/4 h/AC)	Coarse primary α + fine lamellar transformed β (secondary α + retained β)	785	866	9.9
HT (930 °C/1 h/WQ + 550 °C/4 h/AC)	Coarse primary α + decomposed martensite α' + fine dispersed secondary α + β	931	1034	7.5
HT (930 °C/1 h/WQ + 800 °C/2 h/AC)	Coarse primary α + lamellar transformed β + fine dispersed secondary α + β	771	886	16.6
AN (600 °C/2 h/FC)	Lamellar structure	891	976	11.6
AN (834 °C/2 h/FC)	Lamellar structure	856	931	20.4
ST (967 °C/1 h/WQ + FA (590 °C/2 h/AC)	Prior β + martensite α' + fine acicular α	858	918	5.85

Notes: YS — yield strength; UTS — ultimate tensile strength; El — tensile fracture elongation; AD — as deposited; HT — heat-treated; AN — annealed; FC — furnace cooling; AC — air-cooling; RT — room temperature; ST — solution treatment; WQ — water quenching; PA — pre-aging; FA — final aging; v — vertical direction; d — deposition direction.

Fig. 8. Typical microstructures of the Ti-6Al-4V alloy sample produced by WAAM after HIP [36]



The recent results obtained clearly show that post-HIP treatment is the effective method for improving the microstructure and mechanical properties of the Ti-6Al-4V alloy printed parts by WAAM. In general, the HIP was conducted by raising the temperature of the sample well beyond the β phase temperature. The authors [36] first studied the effect of the HIP on the microstructure and tensile properties of Ti-6Al-4V alloy samples produced by WAAM. They used the next HIP regimes: $T = 1200$ K for 2 hrs; $P = 150$ MPa pressure in Ar; $5 \text{ K} \cdot \text{min}^{-1}$ heating and cooling rate. In this work, it was found that HIP starting with the relatively coarse Widmanstätten α in the as-built state would coarsen the microstructure (α/β grain size) and closing porosity (Fig. 8) which may reduce strength while increasing ductility (Table 1). There is an important effect of HIP-induced removing porosity, which improves the fatigue properties. It is understood that internal defects such as porosity considerably reduce fatigue life because they initiate the nucleation process of the surface cracks. Therefore, the size and distribution of porosity will be the critically important factor influencing the fatigue life of Ti-6Al-4V alloy WAAM-ed parts.

The non-HIP-ed (vacuum annealed) component contains spherical porosity, with the largest pore detected throughout the specimen approximately $350 \mu\text{m}$ in diameter. However, it is important to note that large porosity (such as this) is rare and most of the analysed samples either contain no porosity or contain very small pores beyond the resolution of the x-ray equipment. The spherical nature of the porosity indicates that it is most likely entrapped gas porosity. It is unclear where this porosity originates (*i.e.*, argon gas or other) but the highly localized nature of it could suggest that sources may include sections of unclean wire feedstock or substrate. For example, [24] demonstrated that even

Table 5. Average mechanical properties for each test condition [27]

Treatment	0.2% σ_y , MPa	σ_B , MPa	ϵ_f , %
As-printed	710	820	7.18
HIP	712	800	11.0

touching Ti–6Al–4V wire with a human hand before WAAM drastically increased spherical gas porosity with a similar size to the pores observed here. Whatever the source of this localized porosity, it is clear that the HIP processing was very effective in removing it as no porosity was detected after HIP. Additionally, the already coarse-grained α -phase in the as-built WAAM condition continues to coarsen through grain growth during HIP and this further reduces tensile strength.

WAAM is prone to the entrapment of the spherical gas porosity, which ranges in size but can exceed 400 μm in diameter (dimensions measured by x-ray MicroCT). Hot isostatic pressing is very effective in removing the porosity; however, this gave no measurable improvement in strength or ductility (Table 5).

3. Wire + Laser Additive Manufacturing

The laser additive manufacturing process (LAMP) which fabricates Ti–6Al–4V alloy is very popular in recent years and has been most widely used to fabricate complex components in sophisticated fields such as aerospace and medical engineering without substantial machining, resulting in less material waste and reduction in lead-time. Direct laser deposition (DLD) is the type of LAMP that utilizes metal powder/or wire preforms that are directly deposited to the work site accompanied by simultaneous irradiation of the laser beam. The powder-based selective laser melting (SLM) process was first widely developed and applied in manufacturing [42–45].

Early concepts of combining the energy/material delivery for additive manufacture of metals, including DLD, are rooted in the ‘welding AM’ era as evidenced by the patents of Kratky and Harter [46, 47]. Early DLD approaches appeared around 1980, as evidenced by the patent [48] that describes layer-by-layer additive deposition using combined laser-powder (or wire) metallurgy. The robotized LAMP system has been developed at University West (Sweden) in close cooperation with Swedish industry [49].

The present review part focuses on laser metal wire deposition (LMwD), which is the promising AM technique for larger structures with less complexity. The LMwD process exhibits good material quality with low impurity levels and it also exhibits a relatively high deposition rate, *i.e.*, production speed [50] as compared with powder. The central part of LMwD is the generation of the beads using the high-power laser source and additive material in the form of metal wire. The main goal of this part is to get a deeper understanding of the formation mechanism of the microstructure of the 3D printed by LMwD the Ti–6Al–4V samples to achieve excellent mechanical properties.

The laser beam is projected onto the substrate surface and generates the melt pool on the substrate material while the metal wire is fed and

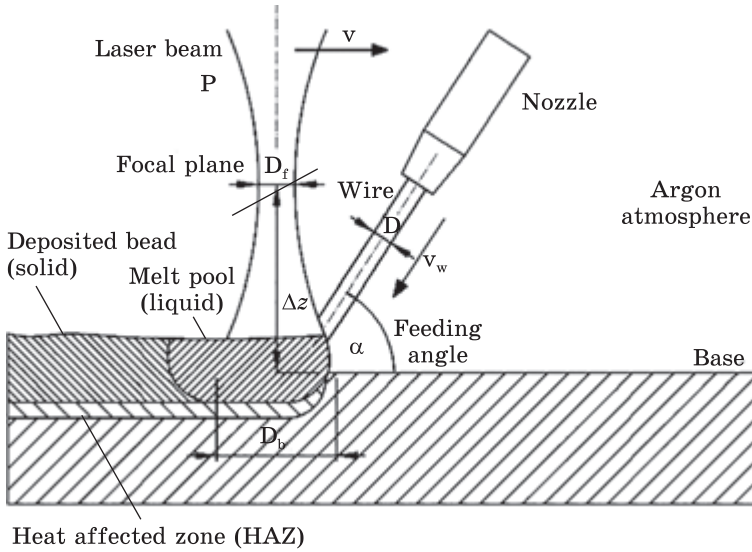


Fig. 9. Schematic view of the laser wire-feed 3D printing [50]

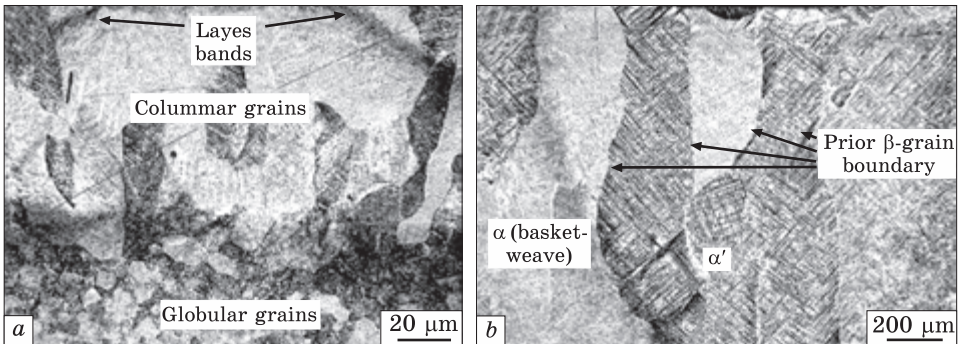


Fig. 10. The SEM microstructure of the laser-printed Ti-6Al-4V alloy samples, where *a* — the bottom area, *b* — the top area [51]

melted, forming the metallurgical contact with the substrate. By moving the laser processing head and the wire feeder, *i.e.*, the welding tool, relative to the substrate the part is formed during solidification. The relative motion of the welding tool and the substrate is made using the 6-axis industrial robot arm. The schematic view of such a printing process in the Ar atmospheres is shown in Fig. 9. The main printing parameters are the laser power, the wire-feed rate, and the traverse speed. Metal is fed by wire, usually, 1.2 mm in diameter, using the standard wire feeding system. It is of importance that the wire-based printing process is sensitive to wire position and orientation relative to the melt pool and the deposition direction. As usually the relatively high-power

laser (e.g., Nd:YAG of wavelength $\lambda = 1064$ nm and a maximum power of 3.5 kW) is utilized to create the molten pool.

The most detailed study of the microstructure of the as printed by LMwD and annealed Ti-6Al-4V alloy samples was completed recently by the authors [51]. They used the Nd:YAG rod laser with the maximum power of 3.5 kW, the Ti-6Al-4V wire diameter 1.2 mm and the Ti-6Al-4V alloy as substrate. It was shown that the as-printed samples have the columnar prior β -grains' morphology that is growing epitaxially across many layers and opposite to the heat flow. With increasing the sample height, the number of grains decreases, and their size increases. Here, the difference was found in the structure of the two regions: top and bottom (Fig. 10). In the bottom area, the grains are partly globular and partly columnar (Fig. 10, *a*) whereas in the top area (Fig. 7, *b*) the grains are fully columnar. It is characteristic that the morphology consists of the curved printed layers. According to the authors [51], this is the result of the heat conduction conditions at a particular location. The detailed analysis showed that the microstructure within the prior β -grains varies to some extent from grain to grain and it consists of the martensite (α') and basket weave α in the as-printed condition. Minor α -phase precipitations at the prior β -grain boundaries are also observed. It was also documented that the stress relieving at 600 °C for 4 h followed by furnace cooling applied to reduce residual stresses resulted in no substantial changes in the microstructure as compared to the as-printed condition.

4. Wire + Electron Beam Additive Manufacturing

A new direction in the development of AM technology based on using the metal wire as feedstock instead of the metal powder and the electron beam as a heating source was patented in the U.S.A. [52, 53]. This new AM technology was named electron beam free form fabrication (EBFFF) or, later, wire electron beam additive manufacturing (WEBAM). In this technology, the 3D objects are formed through layered deposition by electron beam melting of the metal wire tip on the metal substrate. The deposition zone (feed point) is moved with a specified speed relative to the substrate resulting in the solidification of the previously deposited material. The feed point is moved sequentially forming each next layer upon the previous one up to form the complete 3D part predetermined according to the corresponding CAD model. The electron beam falls in EBFFF on the substrate perpendicularly to its surface and feedstock material is fed to the feed point from aside under some angle as can be seen in Fig. 11 [54]. This design uses the electron beam guns of the welding type with a rather high accelerating voltage (60 kV and more). Because of this high voltage, the x-ray radiation from processed parts

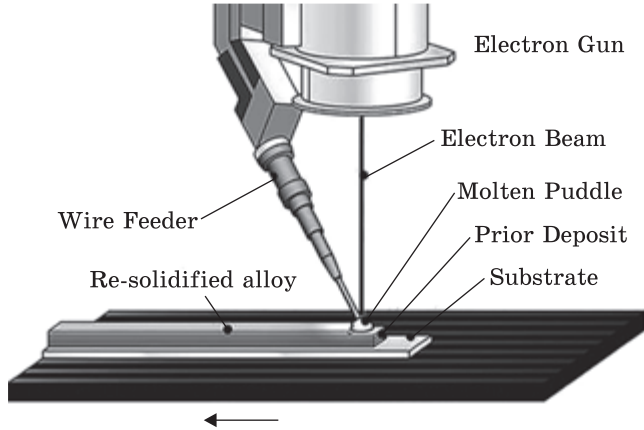


Fig. 11. The concept design of the electron beam free form fabrication [54]

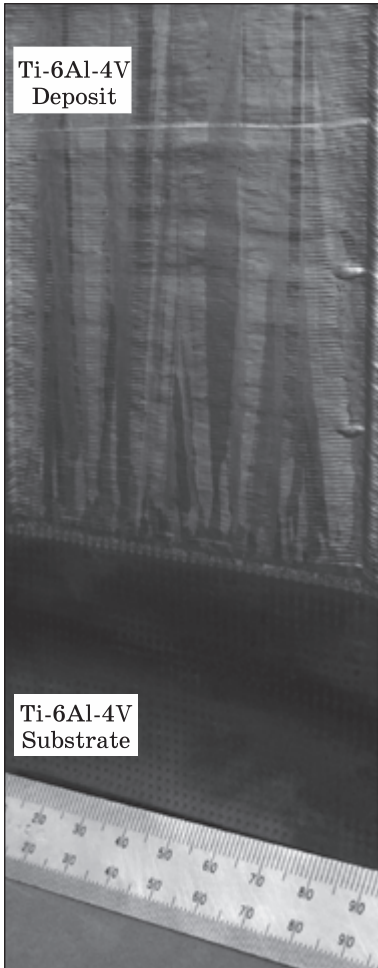


Fig. 12. The Ti-6Al-4V as-printed macrostructure [55]

takes place. As the rule, residual pressure in the operating chamber must be not less than 10^{-1} Pa.

Below there are the recent detailed studies of the macro- and microstructure of the Ti-6Al-4V objects printed by WEBAM with the option of the wire feeding at a certain oblique angle to the substrate.

In the works [55, 56], the WEBAM system was used to evaluate the feasibility of repairing the aero-engine fan blades made of Ti-6Al-4V alloy. This alloy is also used as the substrate and for the wire. The additive repair was conducted using the following AM parameters: the power welding system 42 kW; electron beam gun with the accelerating voltage of 60 kV; the wire diameter 0.9 mm; the wire feedstock was directed axially into the focal point of the electron beam located on the deposited surface; maximum temperatures of 1120 and 1000 °C were recorded for the mid-width and mid-thickness regions, respectively.

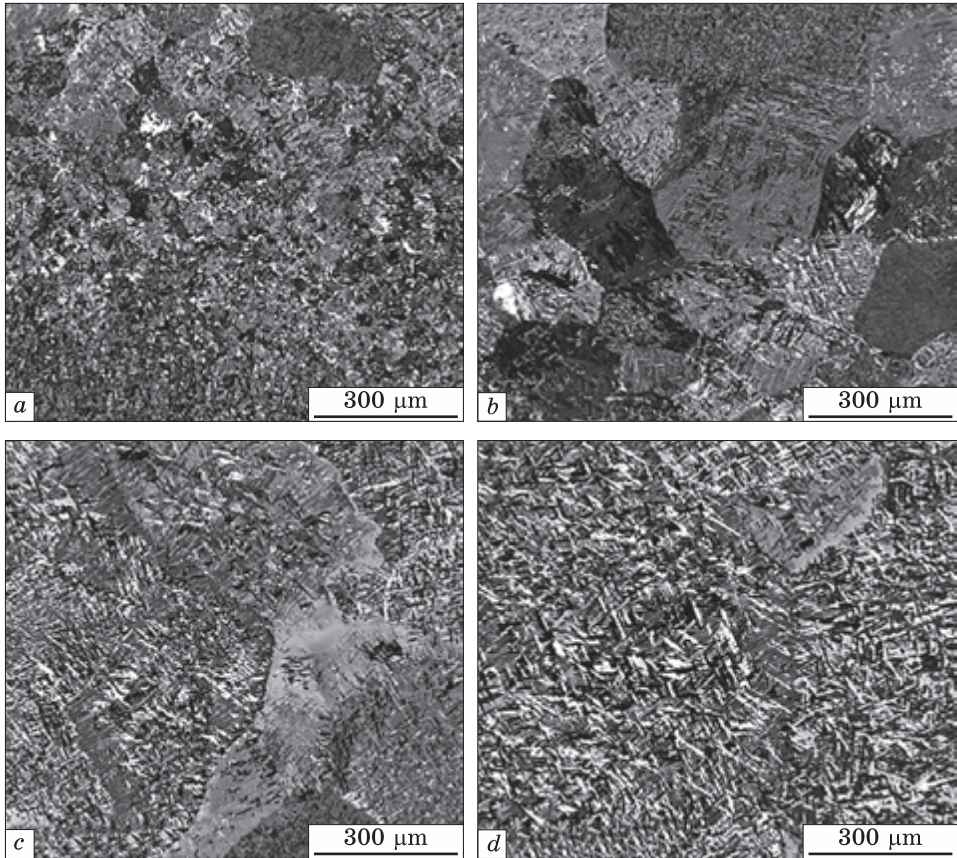


Fig. 13. The microstructure of the Ti-6Al-4V sample printed by WEBAM: *a* — just adjacent to the interface with the substrate; *b* — coarser equiaxed grains in the third layer; *c* — initial columnar grains starting from the fourth layer; *d* — large columnar prior- β grains beyond the fifth layer [55]

The Ti-6Al-4V wall macrostructure of the printed deposit exhibited surfaces that were grey in colour, attributed to the vacuum environment, with periodic contours of the deposited layers, as illustrated in Fig. 12. As can be seen from this figure on the surface of the as-deposited wall, the macrostructure contains the columnar prior β grain boundaries, highlighted by the light and dark grey contrasting regions, originating from the substrate and extending across the deposited layers to the top of the wall. It is obvious that during solidification the preferred growth direction of the columnar prior- β grains was nearly perpendicular to the substrate.

The as-printed microstructure of the first deposited layers is shown in Fig. 13, *a-d*. One can see the bimodal microstructure consisted of fine equiaxed α grains with intergranular and interlamellar β phases. This microstructure is the consequence of the molten wire bead solidifi-

cation into the high temperature β phase, which formed during cooling from the liquidus temperature (1660 °C). The β phase begins to solidify as columnar grains because of the temperature gradient formed between the substrate and printed layers within the first few layers. At the lower 996 °C of the high-temperature β phase allotropic transformation occurs and the low-temperature α phase begins to nucleate at the β grain boundaries through an orientation next relationship: $\{110\}\beta\parallel(0001)\alpha$, $\langle 1120\rangle\alpha\parallel\langle 111\rangle\beta$. At the same time, the 12 primary α phase variants are possible. The nucleated and growth of the α phase as platelets inside the prior- β grains occurs at a further decrease in temperatures. This phase transformation leads to forming the α colonies and the lamellar microstructure complex, which was called $\alpha + \beta$ basket weave. The room temperature microstructures shown in Fig. 13, give evidence of the prior- β grain formation characteristics during the early stages (first few layers) of the WEBAM process. Due to the very fine bimodal microstructure of the titanium alloy substrate, the columnar prior- β grain configuration developed in the deposit through the interface region consisting of the equiaxed prior- β grains (Fig. 13, *a*). Initially, the columnar prior- β grains were comparatively small in size in the layers neighbouring the equiaxed interface region (Fig. 13, *b*, *c*) relative to that in the subsequent layers deposited (Fig. 13, *d*). This gradually gave rise to the columnar prior- β macrostructure visible on the printed sample surface. Comparing Fig. 13, *b* and Fig. 13, *d*, it can be noted that by contrast as the prior- β grains coarsen, the size of the α colonies increases, this, in turn, results in an increase in the α lamellae thickness: small columnar grains — 0.90 μm ; coarse columnar grains — 1.31 μm .

The object of the next study [57] was to establish the suitable parameters for the WEBAM process in $\alpha + \beta$ titanium alloy Ti-6Al-4V and determine the influence of these parameters on the optimal microstructure for the as-deposited and heat-treated building walls. The following 3D deposition parameters were used: wire diameter 1.2 mm, acceleration voltage kV 90, beam current 17.5–46.7 mA, welding speed 9.0–11.0 mm/s, wire feed rate 2.7–3.9 m/min, welding speed 9.0–11.0 mm/s, wire feed rate 2.7–3.9 m/min, the angle between the electron beam and the fed wire 55°, pressure at the working chamber 5×10^{-3} Pa.

Characteristic features of the macrostructural features and the details of the grain boundaries of the AM blocks built by 10 layers \times 5 beads are shown in Figs. 6, *a–d*. Such cross-section demonstrates the features of the epitaxial grown columnar prior β -grains parallel to the build direction, reaching over several layers. The large temperature gradient during the solidification in direction of the heat flow determines the form and size of the columnar prior β -grains. As seen in Fig. 13, *a*, the transition between the printed structure and the substrate consists of coarser equiaxed prior β -grains.

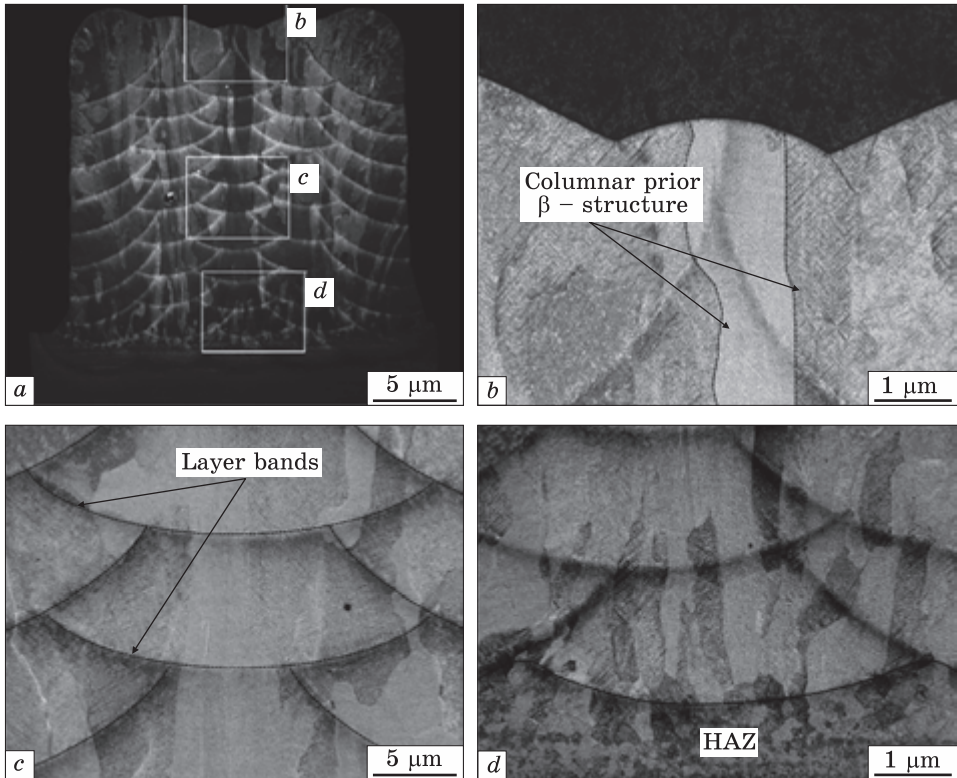


Fig. 14. (a) Macrostructure with layer bands and columnar structure, (b) columnar prior β -grain structure, (c) presence of several layer bands, and (d) transition AM bulk material to heat-affected zone (HAZ) [57]

To provide stress relief in the 3D printed material, post-heat-treatment (PHT) was performed. It was done in the preheated furnace in the atmosphere for 2 h at 710 °C and cooled in still air. As shown in Fig. 14, a, c such the PHT leads to the formation of the mixture microstructure of the finer α and martensite (α') along the whole 3D structure. The morphology of the microstructure is almost homogenous in the whole building block. After the PHT, the microstructure decomposes into the $\alpha + \beta$ structure, with a fine α -lamellar structure (Fig. 14, b). Precipitation of fine β within the fine α lamella detected in Fig. 14, d is due to the heterogeneous enrichment of β -stabilizer elements [57].

The first identification of the layer-by-layer microstructural characteristics in the direction perpendicular to the substrate of the as-received Ti-6Al-4V samples manufactured by WEBAM technology was presented in the research [58]. This will provide the general idea of the predominant microstructure features that should be taken into account when searching for the best configuration in terms of the WEBAM pa-

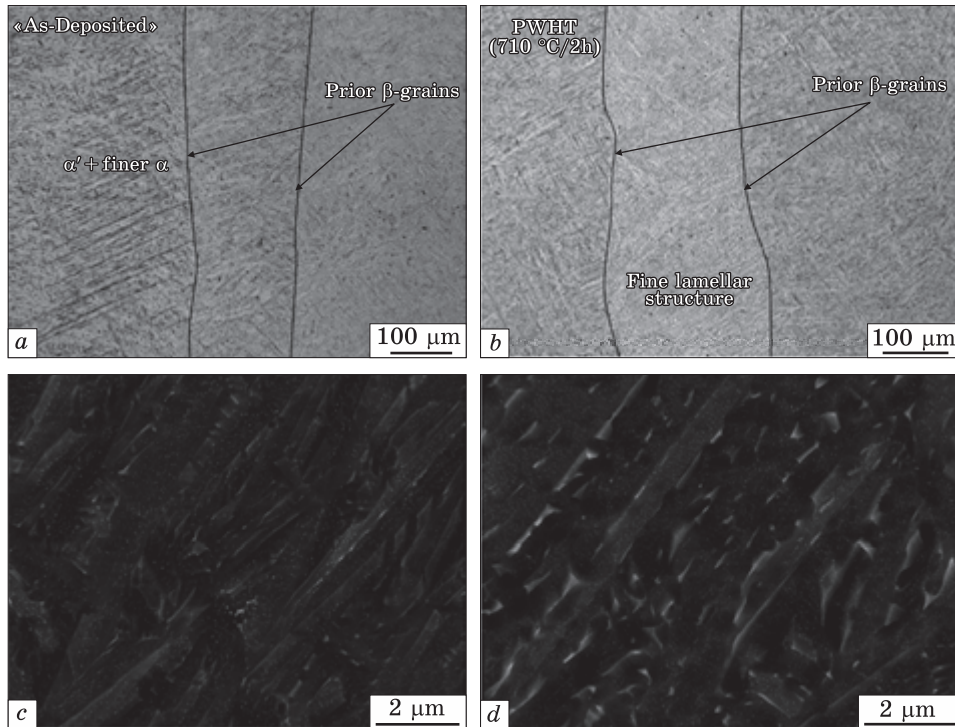


Fig. 15. Microstructure of the AM block centre: (a) as-deposited and (b) after PHT condition; detail of the microstructure by SEM investigations in (c) as-deposited and (d) after PHT conditions [57]

rameters. This data is important to achieve the desired mechanical properties. The present work was performed by manufacturing the single-bead component, which was deposited on the Ti-6Al-4V substrate. The starting wire Ti-6Al-4V material has a 3.2 mm diameter. This high-performance WEBAM system operates in a vacuum (10 Pa). Other AM parameters were not specified.

The cross-section of the macrostructure in the YZ direction of the Ti-6Al-4V WEBAM sample is shown in Fig. 16. One can see the dense macrostructure with no porosities and with three sharp Parts. Part 1 is the Ti-6Al-4V alloy substrate, which is affected by the heat generated due to the deposition of the first layers. At the same time, this region contains the three distinct sub-regions. (1) The base material (BM) region, which is not affected by the indicated generated heat. For this reason, BM microstructure is the same as the as-received material (*e.g.*, globular primary grains elongated in the rolling direction). (2) The heat-affected zone (HAZ), whose peak temperature is sufficiently high but below the β -transus temperature (T_{β} around 995 °C). As the result, there

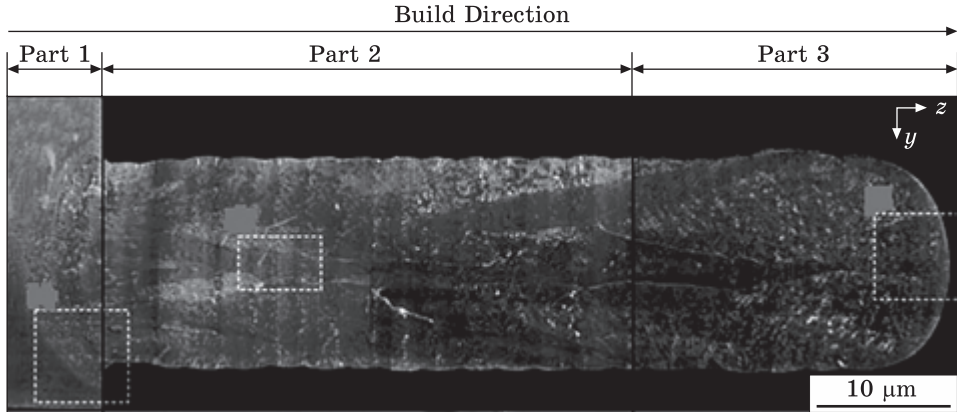


Fig. 16. Macroscopic cross section (YZ plane) of the Ti-6Al-4V WEBAM deposited sample [58]

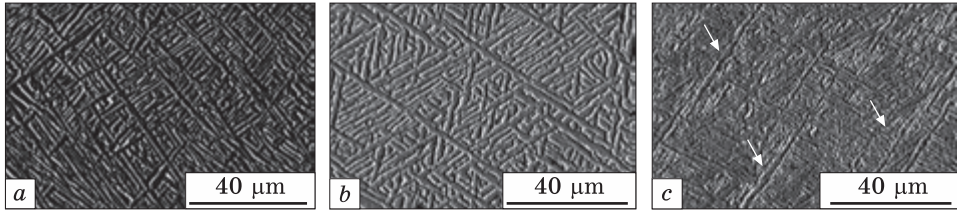


Fig. 17. SEM-BSE images showing the microstructure in the bottom (a), middle (b), and top (c) regions of the deposited wall sample [58]

arise the equiaxed grains, which become bigger from the bottom to the top of this area. (3) The fusion zone (FZ) is also formed at the local temperature higher than T_{β} during the first layer is crystallizes. Here, in Part 3, the large columnar prior β grains begin to grow perpendicularly to the substrate along the multiple layers up to almost the top of the deposit, indicating an epitaxial growth towards the heat flux. In the entire part, the mean prior β grain width increases with the increase in the building height being 0.6 mm, 1.78 mm, and 2.49 mm in the bottom, middle, and top of the deposit, respectively. Part 2 is the region that is reheated below T_{β} when depositing the last layer. It is characterized by the presence of parallel bands, which can be distinguished from the rest of the microstructure by their characteristic colour. Due to thermal cycling effects, these observed bands are another characteristic commonly observed in metal 3D printing. For this reason, in the present work, these bands will be named ‘thermal bands’. At last, Part 3 includes the region where no parallel bands are visible, as it has been entirely heated above the T_{β} when the last layer was deposited. In this case, this region means that the area melted and remelted was very deep

as it went through several layers. Therefore, it is important what the applied heat input to melt the pool in the last layer. Moreover, the presence of a secondary solidification front is seen at the top of this zone where equiaxed grains are observed.

Figure 17 shows the SEM detailed microstructure in three different regions of the deposit wall sample (bottom, middle and top). To avoid any effect that does not represent the general microstructure for the first two variants the images were taken between thermal bands. Such a microstructure is characterized by the heterogeneity along the deposit. As seen in Fig. 17, *a-b*, the basket-weave structure is present in the bottom and middle regions. However, compared to the centre area the microstructure is finer compared to the bottom of the sample. It is because the substrate acts as the thermal sink provoking higher cooling rates in the first layers and therefore, thinner α lamellae thickness is observed. The lamellae size diminution is also the result of the heat accumulation produced during continuous printing, as the heat input is maintained constant throughout the printing process. In the top layer of the deposit, a very fine microstructure is forming (Fig. 17, *c*). The morphology in such area has not been identified with certainty although there appears to be the particle of the α' martensite, as indicated by the arrows in Fig. 17, *c*. The formation of the martensite particles in the top area can indicate that during the printing of the last layer, high cooling rates take place, and neither full decomposition nor coarsening of the microstructure happens, as this area is not reheated.

The determination of the nominal macro- and microstructure is simultaneously supplemented with the analysis of the phase structure formation in the wall sample [58]. This includes the grain boundary α phase which is observed continuously inside the prior β grains in the reheated region, which means that the cooling rates were sufficiently slow for the α phase to be formed and grow. Moreover, the secondary α phase (α_s) is also observed inside the basket-weave microstructure. These α_s precipitate as a consequence of the heating experienced in the $\alpha + \beta$ region during subsequently deposited layers. Another consequence of the heat accumulation in the deposited layers is that α_s volume increases when going towards the middle of the deposited sample. It was concluded that the mean average α lamellae thickness of $1.05 \pm 0.10 \mu\text{m}$ was determined above the thermal bands where the colony microstructure is found.

In recent years, another AM technology of directed energy deposition (DED), which uses the electron beam as the source of melting and the metal wire as feedstock material, becomes distinguished. The fundamental difference between the WEBAM approach and newly rising technology relates to the incidence angle of the wire feeding with respect to the printing part, *i.e.*, perpendicular or oblique. The new AM technology

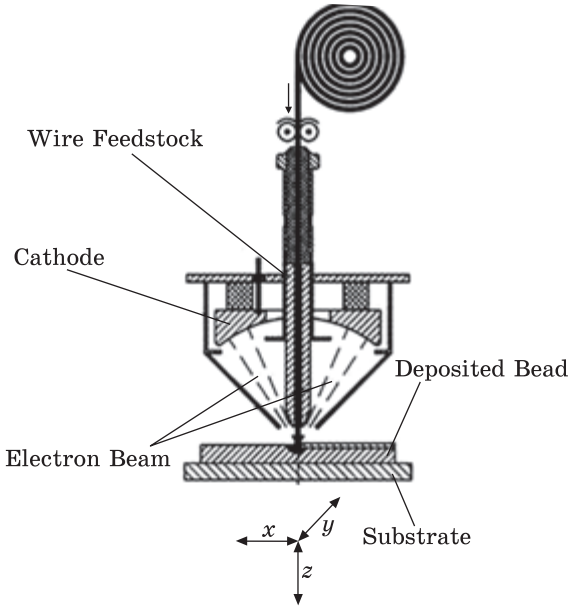


Fig. 18. The schematic diagram of the xB3DMP wire-electron beam device [63]

of the DED type, which employs the unique perpendicular electron beam and coaxial wire feed, has been invented and patented in Ukraine [59]. This AM technology is called ‘xBeam 3D metal printing’ (xB3DMP) due to the construction feature of the electron beam used for melting wire. In the first stage, this new AM technology has been successfully applied for the cost-

efficient manufacturing of the c.p.-Ti and grade 5 (Ti6Al4V) Ti-based alloy parts for various applications [60–63]. According to many experts in the field of AM, the xB3DMP technology is capable to solve many technical and technological problems of the existing additive technologies. First of all, it relates to eliminating the contradiction between manufacturing accuracy and high productivity and thereby providing a radical reduction in the cost of the production the three-dimensional metal parts.

The schematic diagram of the xB3DMP wire-electron beam device is shown in Fig. 18. The characteristic feature of this AM technology is the use of the profile electron beam in the form of the hollow inverted cone as the heating source. It allows coaxial feeding of the consumable wire into the deposition zone. Commonly, wires 2 or 3 mm in diameter were used as the starting material for 3D printing the Ti–6Al–4V alloy. The substrate was the plate of the same alloy. The development of the new method is based on the unique ability of the gas-discharge electron beam guns to generate profile electron beams by direct emission from the cathode without the use of additional deflecting and focusing sifting agents [64]. Also, implementing the technology and achieving positive technological and economic effects are important other characteristic features of gas-discharge electron beam guns, such as the ability to work stably in the wide range of residual pressure in the working chamber (10^{-2} – 10 Pa), including the work in the partial pressure of various inert gases, the ability to generate and form electron beam at the relatively low accelerating voltage (<5 kV). There are key physical and en-

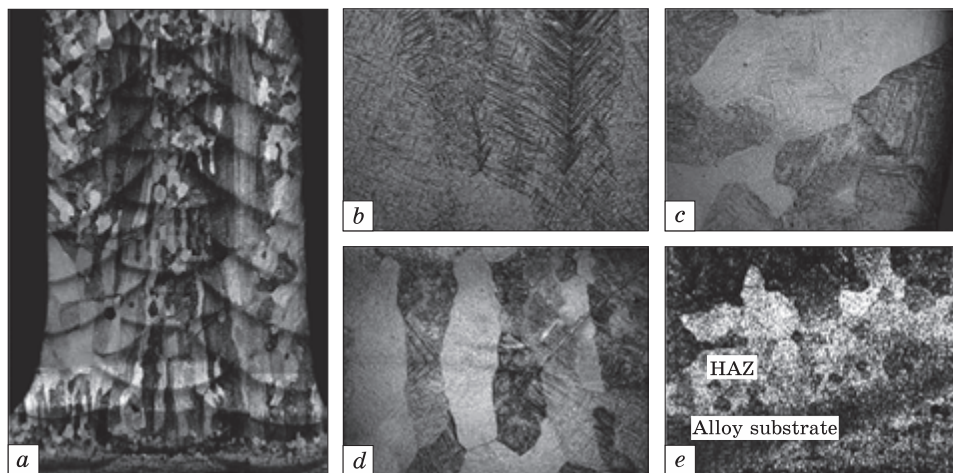


Fig. 19. Macrostructure (a) ($\times 15$) and microstructure (b–e) ($\times 100$) of the transverse (Y–Z) section of the sample, where b — central part, c — the edge of the wall, d — columnar crystals, and e — HAZ [60]

gineering ideas that provide the main technological capabilities to xB3DMP: hollow conical electron beam is used for the creation of a molten pool on the substrate and for melting of feedstock material; feedstock is supplied exactly in the centre of a molten pool through feedstock guide coaxially with an electron beam; a low-voltage gas discharge EB gun and feedstock guide are forming together the common functional assembly. The parameters of the deposited Bead (width and thickness) are easily controlled by changing the power distribution between the wire and substrate by regulating the protrusion between the electron gun and the substrate, also by regulating the substrate speed and the wire feed rate.

Below we present the main results of the macro- and microstructure study of the Ti-6Al-4V alloy single-bead samples produced by AM technology xB3DMP [60–63]. The following technological modes of the AM process were used for the manufacture of the studied samples: power 5.5 kW, accelerating voltage 16 kV, layer thickness 1.6 mm, wire feed speed 16.5 mm/s, substrate movement speed 17 mm, diameter of the titanium wire 2–3 mm.

The macro- and microstructure of the single-bead sample in the Y–Z plane are shown in Fig. 19.

On the metallographic section in the longitudinal and transverse sections, a cast-type macrostructure is visible, consisting of the individual beads (Fig. 19), deposited in three parallel passes. The thickness of the beads is 1.6–2.0 mm. In cross-section, the sample consists of the following zones: the central width of approximately 2.5 mm; two sides,

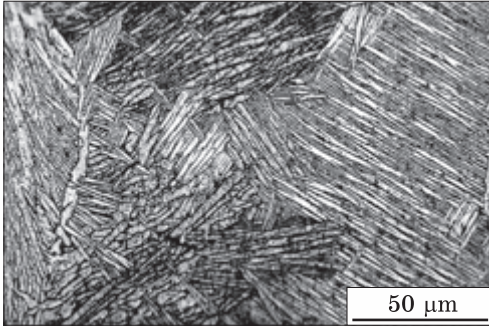


Fig. 20. Microstructure of 3D printed Ti-6Al-4V sample by AM technology xB3DMP [63, 65]

located at the edges of the wall (about 2.0 mm); intermediate, located between the above-mentioned zones with grains having the vertical direction of the crystallization; heat-affected zones (HAZ) of the deposited

metal on the substrate. A cast-type macrostructure is visible, with a predominance of the equiaxed grains (primary structure), consisting of rollers of three parallel passes (Fig. 19, a). The central zone of the ingot formed by the beads of the second pass, 2.5 mm wide, consists of the large grains growing through the boundary of the adjacent deposited layers. The largest grains (260×400, 320×1600 μm), which have a vertical direction of growth, are recorded in the lower beads (Fig. 19, a, b). In the subsequent layers, the grains are smaller and equiaxed, 200–600 μm in size. A similar picture is observed when studying the structure of the longitudinal section of the sample. The investigation of the grain sizes shows that grains formed at the first level adjacent to a cold substrate are noticeably smaller (of about 300 μm) than grains in the core of AM structure. This is due to intensive heat flow towards the cold substrate and significantly faster cooling of the material at the first crystallized bead. Similar grains some smaller than average grain size over AM-produced structures were also formed at the upper crystallized bead due to intensive heat flow via irradiation and faster cooling of such beads. It was concluded that some additional contribution to grain growth inside intermediate layers of the produced material gave heat flow during subsequent melting of neighbouring upper beads.

A detailed study of the secondary microstructure was carried out in the work [62, 63]. The size and aspect ratio (shape) of β grains as well as their inner microstructure should be controlled to achieve an appropriate set of mechanical characteristics. The study of the microstructure in different areas of the printed block demonstrated that the microstructure is quite similar for both the edges and for the central part of the block produced with relatively coarse β grains of about 1 mm in size. Some spherical pores up to 50–60 μm in size are observed in microstructure as defects formed during AM processing. Lamellar α + β intragrain microstructure of as-build blocks is typical for cast Ti-6Al-4V material (Fig. 20). Parallel relatively coarse α lamellae were formed inside β grains on the cooling of each layer below β-transus and further reheating during the printing of the next material layers. Such intragrain

morphology confirms the absence of the martensite-like structure and suggests a moderate level of internal stresses arose in produced material. At the same time, it can be assumed, that the presented $\alpha + \beta$ structure of 3D printed material is not in equilibrium yet due to relatively fast heating and cooling, *i.e.*, thermal cycling. Hence, due to very non-equilibrium conditions under which phase $\beta \leftrightarrow \alpha + \beta$ transformations took place the alloy in various locations can be characterized by different degrees of completeness of the phase transformations. It is important to note that lamellar $\alpha + \beta$ microstructure formed by used AM processing, size of β grains, size of the α colonies inside them, and thickness of α lamellae are the critical parameters affecting mechanical properties [66].

5. Conclusions

Many publications have found that the macro- and microstructure of the Ti-6Al-4V alloy samples of the as-3D printed by various types of AM is very different from that of the conventional technologies. The main reason for this effect is the repeated and rapid thermal cycling that occurs in layer-by-layer 3D printing process. The typical macrostructure in the etched cross-sections of the Ti-6Al-4V alloy sample printed by wire + arc additive manufacturing (WAAM) contains two differently appearing regions, namely the bottom region, which is characterized by bands parallel to the substrate surface, and the top region, where such parallel bands are not detected. In addition to this feature, the macrostructure is characterized by the epitaxial growth of the striking coarse elongated columnar prior- β grains. Latest are formed during solidification and grew almost perpendicular to the top of the sample across the deposited layers. These grains had an average grain width of 1 to 2 mm. In general, the morphology and the size of the columnar prior- β grains significantly depend on the WAAM parameters, namely, wire feed speed, the molten pool size, peak temperature, time at the temperature, and the cooling rate during the multiple thermal cycles experienced by each layer of deposited alloy. Detailed studies have shown that the as-printed microstructure in both regions is characterized by the so-called Widmanstätten structure, which consists of the needle-like α -phase lamellae in the β -phase matrix exhibiting the basket-weave structure and some α lamellae. The main differences between the bottom and top areas are the following: the bottom area contains alternating bands perpendicular to the build direction, while such bands are conversely absent in the top region that contains much finer lamellae and needle-like precipitates than those in the bottom one.

Laser metal wire deposition (LMwD), which is also the promising AM technique for larger structures with less complexity, exhibits a

good material quality with low impurity levels and a relatively high deposition rate. Macroscopically, the morphology consists of curved printed layers. As for the WAAM-produced materials, for the LMwD-made ones, the microstructure of the top and bottom regions is also different. Grains were observed to be partly globular and partly columnar in the bottom area, whereas they are fully columnar in the top area. The microstructure within the prior β -grains varies to some extent from grain to grain and it consists of the martensite (α') and basket weave α in the as-printed condition.

Wire electron beam additive manufacturing (WEBAM) and ‘xBeam 3D metal printing’ (xB3DMP) technologies allow printing 3D objects through the layered deposition by electron beam melting of the metal wire tip on the metal substrate and producing the microstructure dependent on the process parameters. The chosen parameters, *i.e.*, electron beam power, accelerating voltage, layer thickness, the diameter of the titanium wire, wire-feeding speed, and the substrate movement speed, complexly affect the macroscopic and microstructural features of the produced product, and, thus, are the critical parameters affecting mechanical properties. The xB3DMP technology is capable to solve many technical and technological problems eliminating the contradiction between manufacturing accuracy and high productivity and thereby providing a radical reduction in the production cost of 3D metal parts.

It was established that the complex thermal cycles during 3D printing cause the printed component to have the non-uniform distribution of the microstructure, mechanical properties, and large residual stress. To reduce the anisotropy and residual stresses and, therefore, the probability of the cracks’ nucleation, it is necessary to carry out post-processing of the WAAM-printed, LMwD-made or WEBAM-produced objects. Currently, the focus is on two types of such processing, namely, post-heat treatment (PHT) and the post-hot isostatic pressing (PHIP). The stress relieving PHIP was documented to result in no substantial changes in the microstructure as compared to the as-printed condition. Generally, the microstructure after PHT is predominately Widmanstätten/acicular- α . However, the thickness of the α -laths (and β -regions) varies significantly. On the other hand, the solution heat treatment leads to the higher β -fraction which is then quenched to either save the supersaturated β -phase or the appearance of the α' martensite. This single-stage PHT improves the ductility, enhances the strength, eliminates the brittle phase, and refines the grains (*e.g.*, the columnar prior β phase). In addition to post-heat treatment, some other post-treatment techniques such as hot isostatic pressing (HIP) can be used to enhance the performance of 3D printed titanium alloy products. The HIP is now used in the various AM methods, since it allows homogenizing the micro-

structure, eliminating the microspores, and removing defects. Minimizing residual porosity and defects is an important effect of HIP beneficial for improving fatigue properties.

Acknowledgements. The work is supported by the National Academy of Sciences of Ukraine (within the budget program 6541230) and the Ministry of Education and Science of Ukraine (project State Reg. No. 0121U109752).

REFERENCES

1. B. Berman, *Business Horizons*, **55**: 155 (2012);
<https://doi.org/10.1016/j.bushor.2011.11.003>
2. D.L. Rakov and R.Y. Sukhorukov, *J. Mach. Manuf. Reliab.*, **50**: 616 (2021);
<https://doi.org/10.3103/S1052618821070116>
3. T.D. Ngo, A. Kashani, G. Imbalzano, K.T.Q. Nguyen, and D. Hui, *Composites Part B: Eng.*, **143**: 172 (2018);
<https://doi.org/10.1016/j.compositesb.2018.02.012>
4. C.W. Hull, *Method and Apparatus for Production of Three-Dimensional Objects by Stereolithography*, Patent US4575330A, Publ. Mar 11, 1986.
5. J.W. Stansbury, and M.J. Idacavage, *Dent. Mater.*, **32**: 54 (2016);
<https://doi.org/10.1016/j.dental.2015.09.018>
6. P. Wu, J. Wang, and X. Wang, *Automation in Construction*, **68**: 21 (2016);
<https://doi.org/10.1016/j.autcon.2016.04.005>
7. O. Ivanova, C. Williams, and T. Campbell, *Rapid. Prototyp. J.*, **19**: 353 (2013);
<https://doi.org/10.1108/RPJ-12-2011-0127>
8. M. Vaezi, H. Seitz, and S. Yang, *Int. J. Adv. Manuf. Technol.*, **67**: 1721 (2013);
<https://doi.org/10.1007/s00170-012-4605-2>
9. B. Bhushan, and M. Caspers, *Microsyst. Technol.*, **23**: 1117 (2017);
<https://doi.org/10.1007/s00542-017-3342-8>
10. H.D. Nguyen, A. Pramanik, A.K. Basak, Y. Dong, C. Prakash, S. Debnath, S. Shankar, I.S. Jawahir, S. Dixit, D. Buddhi, *J. Mater. Res. Technol.*, **18**: 4641 (2022);
<https://doi.org/10.1016/j.jmrt.2022.04.055>
11. Y.W.D. Tay, B. Panda, S.C. Paul, N.A. Noor Mohamed, M.J. Tan, and K.F. Leong, *Virtual Phys. Prototyping*, **12**: 261 (2017);
<https://doi.org/10.1080/17452759.2017.1326724>
12. L. Mashigo, H. Müller, and C. Gassmann, *J. Southern African Inst. Mining and Metallurgy*, **121**: 325 (2021);
<https://doi.org/10.17159/24119717/1498/2021>
13. S.W. Williams, F. Martina, A.C. Addison, J. Ding, G. Pardal, and P. Colegrove, *Mater. Sci. Technol.*, **32**: 641 (2016);
<https://doi.org/10.1179/1743284715Y.0000000073>
14. D. Ding, Z. Pan, D. Cuiuri, and H. Li, *Robotics and Computer Integrated Manuf.*, **34**: 8 (2015);
<https://doi.org/10.1016/j.rcim.2015.01.003>
15. Z.D. Lin, K.J. Song, and X.H. Yu, *J. Manuf. Proc.*, **70**: 24 (2021);
<https://doi.org/10.1016/j.jmapro.2021.08.018>
16. J.L. Gu, J. Ding, S. W. Williams, H.M. Gu, J. Bai, Y.C. Zhai, and P.H. Ma, *Mater. Sci. Eng. A*, **651**: 18 (2016);
<https://doi.org/10.1016/j.msea.2015.10.101>

17. P.F. Jiang, X.R. Li, X.M. Zong, X.B. Wang, Z.K. Chen, H.X. Yang, C.Z. Liu, N.K. Gao, and Z.H. Zhang, *J. Alloys Compounds*, **920**: 166056 (2022); <https://doi.org/10.1016/j.jallcom.2022.166056>
18. L.E. Murr, S.M. Gaytan, A. Ceylan, E. Martinez, J.L. Martinez, D.H. Hernandez, B.I. Machado, D.A. Ramirez, F. Medina, S. Collins, and R.B. Wicker, *Acta Mater.*, **58**: 1887 (2010); <https://doi.org/10.1016/j.actamat.2009.11.032>
19. S.W. Williams, F. Martina, A.C. Addison, J. Ding, G. Pardal, and P. Colegrove, *Mater. Sci. Technol.*, **32**: 641 (2016); <https://doi.org/10.1179/1743284715Y.0000000073>
20. D.H. Ding, Z.X. Pan, D. Cuiuri, and H.J. Li, *J. Adv. Manuf. Technol.*, **81**: 465 (2015); <https://doi.org/10.1007/s00170-015-7077-3>
21. S.Yu. Tarasov, A.V. Filippov, N.L. Savchenko, S.V. Fortuna, V.E. Rubtsov, E.A. Kolubaev, and S.G. Psakhie, *Int. J. Adv. Manuf. Technol.*, **99**: 2353 (2018); <https://doi.org/10.1007/s00170-018-2643-0>
22. C.R. Cunningham, J.M. Flynn, A. Shokrani, V. Dhokia, and S.T. Newman, *Additive Manuf.*, **22**: 672 (2018); <https://doi.org/10.1016/j.addma.2018.06.020>
23. D.H. Ding, Z.X. Pan, D. Cuiuri, and H.J. Li, *Int. J. Adv. Manuf. Technol.*, **81**: 465 (2015); <https://doi.org/10.1007/s00170-015-7077-3>
24. F. Wang, S. Williams, P. Colegrove, and A.A. Antonysamy, *Metall. Mater. Trans. A*, **44**: 968 (2013); <https://doi.org/10.1007/s11661-012-1444-6>
25. F. Martina, J. Mehnen, S.W. Williams, P. Colegrove, and F. Wang, *J. Mater. Process. Technol.*, **212**: 137 (2012); <https://doi.org/10.1016/j.jmatprotec.2012.02.002>
26. B. Baufeld, O. van der Biest, and R. Gault, *Int. J. Mat. Res.*, **100**: 11 (2009); <https://doi.org/10.3139/146.110217>
27. B. Baufeld, O. van der Biest, R. Gault, and K. Ridgway, *IOP Conf. Ser.: Mater. Sci. Eng.*, **26**: 012001 (2011); <http://dx.doi.org/10.1088/1757-899X/26/1/012001>
28. J. Zhang, X.Y. Wang, S. Paddea, and X. Zhang, *Mater. Des.*, **90**: 551 (2016); <http://dx.doi.org/10.1016/j.matdes>
29. F. Wang, S. Williams, P. Colegrove, and A.A. Antonysamy, *Metall. Mater. Trans. A*, **44**: 968 (2013); <https://doi.org/10.1007/s11661-012-1444-6>
30. Q. Wu, J.P. Lu, C.M. Liu, H.G. Fan, X.Z. Shi, J. Fu, and S. Ma, *Materials*, **10**: 749 (2017); <https://doi.org/10.3390/ma10070749>
31. J. Wang, X. Lin, M. Wang, J.Q. Li, C. Wang, and W.D. Huang, *Mater. Sci. Eng. A*, **776**: 139020 (2020); <https://doi.org/10.1016/j.msea.2020.139020>
32. Z.D. Lin, K.J. Song, and X.H. Yu, *J. Manuf. Proc.*, **70**: 24 (2021); <https://doi.org/10.1016/j.jmapro.2021.08.018>
33. C.M. Liu, H.M. Wang, X.J. Tian, H.B. Tang, and D. Liu, *Mater. Sci. Eng. A*, **586**: 323 (2013); <https://doi.org/10.1016/j.msea.2013.08.032>
34. C.M. Liu, H.M. Wang, X.J. Tian, and D. Liu, *Mater. Sci. Eng. A*, **604**: 176 (2014); <https://doi.org/10.1016/j.msea.2014.03.028>

35. B. Baufeld, O. Van der Biest, and S. Dillien, *Metall. Mater. Trans. A*, **41**: 1917 (2010);
<https://doi.org/10.1007/s11661-010-0255-x>
36. M.J. Bermingham, L. Nicastro, D. Kent, Y. Chen, and M.S. Dargusch, *J. Alloys Compounds*, **753**: 247 (2018);
<https://doi.org/10.1016/j.jallcom.2018.04.158>
37. A. du Plessis and E. Macdonald, *Additive Manuf.*, **34**: 101191 (2020);
<https://doi.org/10.1016/j.addma.2020.101191>
38. M.B. Berger, T.W. Jacobs, B.D. Boyan, and Z. Schwartz, *J. Biomed. Mater. Res. B Appl. Biomater.*, **108**: 1262 (2020);
<https://doi.org/10.1002/jbm.b.34474>
39. V. Popov, A. Katz-Demyanetz, A. Garkun, G. Muller, E. Strokin, and H. Rosen-son, *Proc. Manuf.*, **21**: 125 (2018);
<https://doi.org/10.1016/j.promfg.2018.02.102>
40. N. Eshawish, S. Malinov, W. Sha, and P. Walls, *J. Mater. Eng. Perform.*, **30**: 5290 (2021);
<https://doi.org/10.1007/s11665-021-05753-w>
41. S.N. Liu, and Y.C. Shin, *Mater. Des.*, **164**: 107552 (2019);
<https://doi.org/10.1016/j.matdes.2018.107552>
42. Z. Zhao, J. Chen, X.F. Lu, H. Tan, X. Lin, and W.D. Huang, *Mater. Sci. Eng. A*, **691**: 16 (2017);
<http://dx.doi.org/10.1016/j.msea.2017.03.035>
43. M. Thoms, G.J. Baxter, I. Todd. *Acta Mater.*, **108**: 26 (2016);
<https://doi.org/10.1016/j.actamat.2016.02.025>
44. T. Wang, Y.Y. Zhu, S.Q. Zhang. *J. Alloys Compounds*, **632**: 513 (2015);
<https://doi.org/10.1016/j.jallcom.2015.01.256>
45. B.E. Carroll, T.A. Palmer, A.M. Beese., *Acta Mater.*, **87**: 309 (2015);
<https://doi.org/10.1016/j.actamat.2014.12.054>
46. A. Kratky, *Production of Hard Metal Alloys*, Patent US2076952, Publ. Apr. 13, 1937.
47. I. Harter, *Method of Forming Structures Wholly of Fusion Deposited Weld Metal*, Patent US2299747A, Publ. Oct. 27, 1942.
48. C.O. Brown, E.M. Breinan, and B.H. Kear, *Method for Fabricating Articles by Sequential Layer Deposition*, Patent US4323756A, Publ. Apr. 06, 1982.
49. A. Heralić, A.-K. Christiansson, M. Ottosson, and B. Lennartson, *Opt. Laser. Eng.*, **48**: 478 (2010);
<https://doi.org/10.1016/j.optlaseng.2009.08.012>
50. E. Brandl, F. Palm, V. Michailov, B. Viehweger, and C. Leyens, *Mater. Des.*, **32**: 4665 (2011);
<https://doi.org/10.1016/j.phpro.2010.08.087>
51. E. Brandl, A. Schoberth, and C. Leyens, *Mater. Sci. Eng. A*, **532**: 295 (2012);
<https://doi.org/10.1016/j.msea.2011.10.095>
52. D.S. Henn, *Solid Freeform Fabrication System and Method*, US Patent 7073561, Publ. Jul. 11, 2006.
53. K.M. Taminger, J.K. Watson, R.A. Hafley, and D.D. Petersen, *Solid Freeform Fabrication Apparatus and Methods*, Patent US7168935 B1, Publ. Jan 30, 2007.
54. S.V. Fortuna, A.V. Filippov, E.A. Kolubaev, A.S. Fortuna, and D.A. Gurianov, *AIP Conf. Proc.*, **2051**: 020092 (2018);
<https://doi.org/10.1063/1.5083335>
55. P. Wanjara, K. Watanabe, C. de Formanoir, Q. Yang, C. Bescond, S. Godet, M. Brochu, K. Nezaki, J. Gholipour, and P. Patnaik, *Adv. Mater. Sci. Eng.*, **2019**:

- 3979471 (2019);
<https://doi.org/10.1155/2019/3979471>
56. P. Wanjara, J. Gholipour, E. Watanabe, K. Watanabe, T. Sugino, P. Patnaik, F. Sikan, and M. Brochu, *Adv. Mater. Sci. Eng.*, **2020**: 1902567 (2020);
<https://doi.org/10.1155/2020/1902567>
57. F. Pixner, F. Warchomicka, P. Peter, A. Steuwer, M.H. Colliander, R. Pederson, and N. Enzinger, *Materials*, **13**: 3310 (2020);
<https://doi.org/10.3390/ma13153310>
58. S. Lopez-Castaco, P. Emile, C. Archambeau, F. Pettinari-Sturmel, and J. Douin. *TMS 2021 150th Annual Meeting & Exhibition Supplemental Proceedings. The Minerals, Metals & Materials Series. Springer, Cham.*
https://doi.org/10.1007/978-3-030-65261-6_16
59. D.V. Kovalchuk, V.I. Melnik, I.V. Melnik and B.A. Tugaj, *Method for Manufacturing Three-Dimensional Objects and Devices for Its Implementation*, UA Patent 112682 C2, Ukraine, Publ. Oct. 10, 2016, Bulletin No. 19 (in Ukrainian).
60. D.V. Kovalchuk, G.M. Grigorenko, A.Yu. Tunik, L.I. Adeeva, S.G. Grigorenko, and S.N. Stepanyuk, *Electrometallurgy Today*, No. 4: 62 (2018) (in Russian);
<https://doi.org/10.15407/sem2018.04.05>
61. D.V. Kovalchuk, V.I. Melnik, I.V. Melnik and B.A. Tugaj, *Automatic Welding*, No. 12: 26 (2017) (in Russian);
<https://doi.org/10.15407/as2017.12>
62. D. Kovalchuk, O. Ivasishin, and D. Savvakina, *MATEC Web of Conferences*, **321**: 03014 (2020);
<https://doi.org/10.1051/mateconf/202032103014>
63. D. Kovalchuk, V. Melnyk, I. Melnyk, D. Savvakina, O. Dekhtyar, O. Stasiuk, and P. Markovsky, *J. Mater. Eng. Perform.*, **30**: 5307 (2021);
<https://doi.org/10.1007/s11665-021-05770-9>
64. D. Kovalchuk, V. Melnyk, I. Melnyk, and B. Tugaj, *J. Elektrotechnica & Elektronica*, **51**, Nos. 5–6: 37 (2016);
<https://epluse.ceec.bg/wp-content/uploads/2018/08/20160506-full.pdf>
65. O.M. Ivasishin D.V. Kovalchuk, P.E. Markovsky, D.G. Savvakina, O.O. Stasiuk, V.I. Bondarchuk, D.V. Oryshych, S.G. Sedov, and V.A. Golub, *Prog. Phys. Met.*, **24**, No. 1: 75 (2023);
<https://doi.org/10.15407/ufm.24.01.075>
66. M.O. Vasylyev, B.M. Mordyuk, and S.M. Voloshko, *Prog. Phys. Met.*, **24**, No. 1: 38 (2023);
<https://doi.org/10.15407/ufm.24.01.038>

Received 19.08.2022;
in final version, 23.01.2023

М.О. Васильєв¹, Б.М. Мордюк^{1,2}, С.М. Волошко²

¹ Інститут металофізики ім. Г.В. Курдюмова НАН України,
бульв. Академіка Вернадського, 36, 03142 Київ, Україна

² Національний технічний університет України
«Київський політехнічний інститут імені Ігоря Сікорського»,
просп. Перемоги, 37, 03056 Київ, Україна

АДИТИВНЕ ВИРОБНИЦТВО СТОПУ Ti-6Al-4V НА ОСНОВІ ПОДАВАННЯ ДРОТУ. ЧАСТИНА I. МІКРОСТРУКТУРА

Останніми роками адитивне виробництво (АВ) металів, також відоме як 3D-друк, виросло в значну галузь. Здатність АВ створювати деталі безпосередньо з цифрових моделей робить його чудовою альтернативою порівняно з традиційними виробничими технологіями, такими як фрезерування, зварювання, литво, прокатка, штампування, кування та токарне оброблення для швидкого виготовлення замовних деталей. В даний час розроблено ряд різних порошкових і дротяних АВ-технологій 3D-друку металів. Було відзначено низку потенційних переваг АВ, включаючи довільність проектування, виготовлення складних деталей, зменшення відходів матеріалу та ваги деталей, мінімізацію використання матеріалів, а також економію часу та грошей для виробничого циклу. Завдяки доцільності економічного виробництва великомасштабних металевих компонентів з відносно високою швидкістю осадження, низькою вартістю обладнання, високою ефективністю матеріалів і скороченим часом виконання в порівнянні з порошковим АВ дротяне АВ приваблює значну увагу в промисловості та наукових колах через його здатність виробляти великі компоненти середньої геометричної складності. Під час процесу АВ дріт подається з контрольованою швидкістю у ванну розтопу, утворену електричною дугою, лазером або електронним променем як джерелом тепла. В останні кілька десятиліть фундаментальні дослідження та розробки спрямовані на 3D-друк на основі дроту деталей, виготовлених зі стопу Ti-6Al-4V, який широко досліджувався та використовувався в різних галузях, таких як аерокосмічна, автомобільна, енергетична, морська промисловості та на додаток до протезування й ортопедичних імплантатів. Численні дослідження впливу параметрів 3D-друку останніх років показали істотну різницю в механізмі та кінетиці формування мікроструктури у зразках стопу Ti-6Al-4V порівняно з традиційними технологіями. Було добре досліджено, що механічні властивості такого стопу залежать від макро- та мікроструктури твердіння, яка контролюється тепловими умовами під час 3D-друку. У даному огляді проаналізовано основні мікроструктурні характеристики, що визначають механічні властивості двофазного стопу Ti-6Al-4V, для зразків, одержаних методом 3D-друку з подачею дроту з використанням різних джерел його топлення, а саме, електричної дуги, лазера й електронного променя. По-перше, оглянуто зв'язки між параметрами процесу, одержаними мікроструктурами, особливо морфологією, розміром і кількісним співвідношенням α - і β -зерен у зразках стопу Ti-6Al-4V після друку. Однак металеві вироби, виготовлені за допомогою переважної більшості процесів АВ, потребують подальшого оброблення шляхом термічного оброблення та/або гарячого ізостатичного пресування, які також обговорюються в цьому огляді.

Ключові слова: адитивне виробництво, 3D-друк, стоп Ti-6Al-4V, мікроструктура, електрична дуга, лазер, електронний промінь, кристалізація, термооброблення, механічні властивості, промисловість.